Journal of
Materials Chemistry A

Materials for energy and sustainability

Accepted Manuscript

This article can be cited before page numbers have been issued, to do this please use: G. Pagot, M. Bandiera, K. Vezzu', A. Migliori, R. Bertoncello, E. Negro, V. Morandi and V. Di Noto, *J. Mater. Chem. A*, 2020, DOI: 10.1039/D0TA06865A.

ROYAL SOCIETY OF CHEMISTRY

rsc.li/materials-a

View Article Online
DOI: 10.1039/D0TA06865A

ARTICLE

High Valence Transition Metals Doped Olivine Cathodes for Superior Energy and Fast Cycling Lithium Batteries

Received 00th January 20xx,
Accepted 00th January 20xx

DOI: 10.1039/x0xx00000x

Gioele Pagot,*[a,b] Marco Bandiera, [a,b] Keti Vezzù, [a,b] Andrea Migliori, [c] Renzo Bertoncello, [d] Enrico Negro, [a,b] Vittorio Morandi, [c] and Vito Di Noto*[a,b]

Mixed-metals olivine cathode materials are one of the most promising systems in the field of lithium batteries. Their main drawback is the low electronic conductivity, which limits the current rate at which they can be cycled. Here, the effect on the electrochemical properties of vicariant high-valence transition metals (HVTMs) inserted in the olivine crystal structure is studied. The strategy here adopted consists in doping a $LiFe_{1/3}Ni_{1/15}Co_{3/5}PO_4$ cathode by substituting part of the cobalt(II) ions with vanadium(IV), niobium(V), or tantalum(V) HVTMs. WAXD studies reveal that small HVTMs molar quantities (HVTM/P = 0.04) are vicariant into the olivine crystal lattice. Single-cell tests show for Nb-doped cathode a high-voltage (*ca*. 4.5 V) and a specific capacity of 149 mAh g^{-1} (656 mWh g^{-1}). Thus, the insertion in the cathode structure of HVTMs exceptionally rises the electric conductivity of the material and yields an improved cyclability and rate capability owing to its electro-compensation effect.

Introduction

A new era is arising in the automotive field, where fueled-power vehicles are going to be banned and electric vehicles (EVs) are becoming the only technology for public and private transportation.[1] In this scenario, secondary batteries play a crucial role in the storage technology owing to their highest efficiency in the electrochemical energy conversion processes. Amongst them, Li-ion batteries are up to day considered the most reliable devices to power EVs thanks to their high energy density.[2-4] Nevertheless, in EVs applications the performances exhibited by Li-ion batteries are still inadequate to sustain a driving range higher than 550 km, due to their insufficient specific energy.[5] Two different approaches are thus suggested to improve their specific energy (*i.e*. capacity × voltage *per* unit of mass): (i) the use of lithium metal as anode; and (ii) the development of high-voltage and high-capacity cathode materials. The former target, due to safety and stability issues which exist at the interface between Li metal and the electrolyte, is mainly pursued by synthetizing suitable polymer or inorganic solid-state electrolytes.[6-11] In the last decades, the latter target triggered the development of a huge number of cathode materials, such as $LiCoO_2$ (LCO), $LiFePO_4$ (LFP), $LiMn_2O_4$ (LMO), $LiNi_xMn_yCo_{1-x-y}O_2$ (NMC), and $LiNi_xCo_yAl_{1-x-y}O_2$ (NCA).[12, 13] Among these, the highest specific energy values are shown by both NMC and NCA (*ca*. 740 mWh g^{-1}).[14] Nevertheless, these cathodes demonstrate an average discharge potential of *ca*. 3.7 V, that limits their specific power, and present severe stability issues which still need to be addressed.[14] On the other hand, the olivine $LiFePO_4$ cathodic material, with its specific energy of *ca*. 620 mWh g^{-1}, is considered a valid alternative to the other systems thanks to its good stability, safety, low environmental impact and easiness of synthesis.[15] In addition, the electrochemical features of this olivine cathode (*e.g*. working potential, capacity, efficiency, etc.) can be significantly modulated by substituting part of the Fe^{2+} ions with other M^{2+} transition metals such as Mn^{2+}, Co^{2+}, or Ni^{2+}.[16-18] Unfortunately, olivine cathodes based on divalent metals (LMP) show poor electronic and ionic conductivities, which limit their rate capability.[19] Recent studies reported that this issue can be mitigated by doping an olivine material with High Valence Transition Metals (HVTMs), such as vanadium.[20-22] In this case the improvement in performance is interpreted in terms of the so called "*charge compensation effect*" which, in LM_1M_2P cathodes, consists in the neutralization with very mobile electrons of the charge difference originated in the 3D-structure by the presence of M_1 (IV or V oxidation state) and M_2 (II oxidation state) metal ions. For "*vicariant*" vanadium in the 3D iron olivine structure, the incorporation mechanism is represented by the following defect equation:[21]

$$VO_2 + Fe_{Fe}^{x} \rightarrow V_{Fe}^{\cdot\cdot} + 2e^- + FeO + \frac{1}{2}O_2 \qquad (1)$$

Mobile electrons are also released in the case that HVTM dopants are inserted into the lithium sites, according to the equation:[23]

$$VO_2 + Li_{Li}^{x} \rightarrow V_{Li}^{\cdot\cdot\cdot} + 3e^- + \frac{1}{2}Li_2O + \frac{3}{4}O_2 \qquad (2)$$

Other mechanisms have been proposed in the literature in addition to the electron formation in order to describe the substitution mechanisms of HVTM dopant ions into the olivine crystal lattice. In details, the HVTM insertion could trigger the formation of Li^+ or M^{2+} vacancies, with the consequent release of several (depending on the charge of the HVTM) Li^+/M^{2+} ions *per* HVTM inserted.[23-25] These latter mechanisms are less likely due to entropic unbalance which arises, even though they can not be excluded. Indeed, in the charge compensation mechanism resulting from the electron formation (Eq.

[a] Section of Chemistry for the Technology (ChemTech), Department of Industrial Engineering, University of Padova, Via Marzolo 9, I-35131 Padova (PD), Italy. E-mail: vito.dinoto@unipd.it. E-mail: gioele.pagot@unipd.it.
[b] Centro Studi di Economia e Tecnica dell'Energia Giorgio Levi Cases, Via Marzolo 9, I-35131 Padova (PD), Italy.
[c] National Research Council of Italy, Institute for Microelectronics and Microsystems – CNR IMM Section of Bologna, via Gobetti 101, I-40129 Bologna (BO), Italy.
[d] Department of Chemical Sciences, University of Padova, Via Marzolo 1, I-35131 Padova (PD), Italy.
† Electronic Supplementary Information (ESI) available. See DOI: 10.1039/x0xx00000x

Scheme 1. Synthesis pathways (I, II and III) of cathode materials. I, completely oxidizing atmosphere. II, partial reducing environment by adding graphite. III, full reducing environment by flowing a N_2/H_2 gas mixture. Group A includes LFNCVP, LFNCVP/C, and LFNCVP/H materials, while B comprises LFNCNP and LFNCTP systems which are synthetized following pathway I and doped with Nb and Ta, respectively.

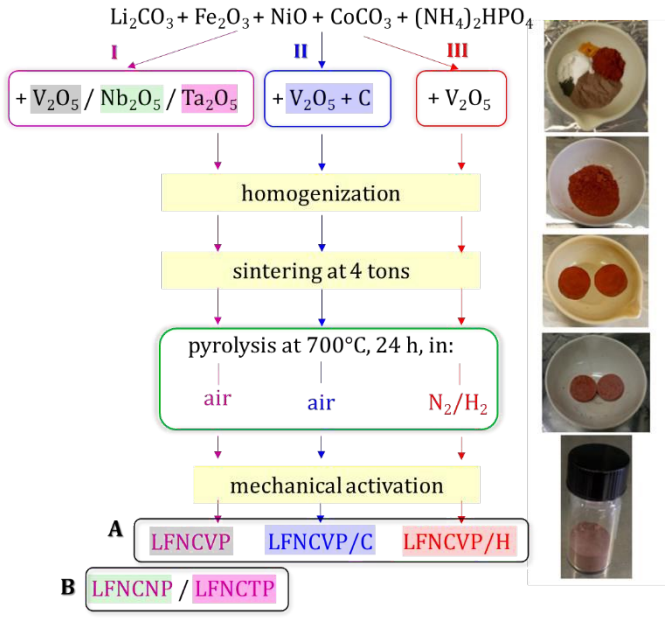

1 and 2) a 1:1 ion exchange (HVTM: Li^+/M^{2+}) occurs, thus the entropy of the crystal system is constant and electrons are easier to be released. It is demonstrated that the charge compensation effect, which acts to improve the bulk electrical conductivity of the olivine cathodes, increases linearly as the concentration of V in materials is raised.[21]

Here, the aim is to explore the effect of HVTM (*i.e.* V(IV), Nb(V) and Ta(V)) doping of LFNCP material on the electrochemical and chemico-physical properties of the resulting cathodes. This target is pursued at first optimizing the synthesis protocol and secondly, by using the optimized preparation pathway, mixed metal olivines doped with V, Nb and Ta are prepared. These investigations are crucial in order to reveal the correlation existing between the "*charge compensation effect*" induced in the proposed cathodes by these metals and their electrochemical properties both "*ex situ*" and "*in situ*" in coin cell batteries.

Results and discussion

Synthesis and stoichiometry.

To investigate the effect of HVTM doping on the electrochemical performance of LFNCP materials, three groups of cathodes (I, II, and III) are prepared following Scheme 1. As anticipated in the Introduction, the strategy adopted consists: A) in optimizing the material synthesis by doping the LFNCP olivines with vanadium as shown in I, II, and III preparation pathways (Scheme 1); and B) in the preparation of Nb- and Ta-doped olivines, by using the optimized synthesis route (I). In A, three different V-doped materials, labeled LFNCVP, LFNCVP/C and LFNCVP/H, are obtained (group A of Tab. 1 and Scheme 1) by gradually increasing the degree of reducing environment in the synthesis process. In details, the preparation of group A materials is carried out as follows. V_2O_5 is mixed with the other reagents in a planetary ball mill. The obtained powder is sintered in a pellet and then pyrolyzed in the selected atmosphere at 700°C for 24 h (see details reported in the Experimental section). In II, the reducing environment is increased by adding 5 wt% of carbon black, while in III it is raised by pyrolyzing the material under a 10 vol% of H_2 in N_2 atmosphere. The best electrochemical performance is obtained by I route (see Electrochemical studies and Battery tests sections), which is adopted to synthetize the other mixed metal olivines doped with Nb and Ta (see group B of Tab. 1 and Scheme 1). The composition of A and B materials is shown in Tab. 1. Fe, Ni, and Co molar ratios are in accordance with the stoichiometry of LFNCP reference material (R).[18] It results that the typical olivine structure is preserved when materials exhibit a molar ratio HVTM/PO_4 (*i.e.*, with HVTMs = V, Nb, and Ta) lower than 0.07.[20, 21, 26, 27] Indeed, segregated $Li_3V_2(PO_4)_3$ phases are revealed when the V/PO_4 molar ratio is higher than 0.07.[21] In LFNCVP and LFNCVP/H, ICP-AES analyses show an excess of lithium. This is in accordance with other studies and suggests that M^{n+} ions in proposed materials are substituted by Li^+ in their octahedral sites (*anti-site* substitution effect).[25] In addition their phosphate deficiency is primarily associated to the presence in bulk materials of metal oxide traces (see Structure section), which slightly reduces the complete conversion of reagents to the desired olivine products. CHNS-O results confirm that in LFNCVP/C the carbon fraction is completely oxidized.

Further insights on the surface chemical composition of materials are obtained by X-ray photoelectron spectroscopy (XPS) studies. XPS peaks (see Fig. S1, ESI†) are revealed at the typical BE values expected for the elements composing the cathodic materials.[28] The intensities centered at 712 and 726 eV with no satellite peaks are attributed to Fe^{2+} ions of an olivine-like structure.[21] In these spectra, traces of Fe^{3+} resulting from the unreacted Fe_2O_3 cannot be excluded at the detection limit of XPS analyses.[29, 30] Peaks with a low intensity at the typical BE values of nickel ions are detected.[18] The two peaks centered at 782 and 798 eV, which are coupled with their relative shake-up peaks, are attributed to the typical Co^{2+} features of olivine materials.[18, 31] In vanadium- doped samples, it is interesting to note the broadening of the $V_{2p3/2}$ peak at 517 eV, which demonstrates the coexistence in samples of both vanadium V and IV oxidation states.[32, 33] The $V_{2p3/2}$ peak is decomposed with two intensities peaking at 517.4 eV and 516.5 eV, ascribed respectively to vanadium V and vanadium IV[32] (see Fig. S2, ESI†). Materials of A group show that: (i) the relative intensity of the vanadium IV component on the surface increases as the degree of reducing environment of the pyrolysis process is raised, in the order LFNCVP < LFNCVP/C < LFNCVP/H; (ii) the here adopted synthetic routes are very effective to prepare mixed metal 3D-olivines doped with V. In LFNCNP sample (group B), the typical peak of Nb^{5+} ion is revealed which is vicariant in the 3D structure of an olivine-like material.[34] Unfortunately, the $Ta_{4f7/2}$ and $Ta_{4f5/2}$ peaks of LFNCTP, which are expected at 25 and 28 eV, respectively, are overlapped to the intense O_{2s} peak, thus only a shoulder signal attributed to $Ta_{4f7/2}$ is measured.[28, 35] Finally, a weak C_{1s} peak is present in the spectra, which is attributed to the presence of adventitious carbon.

View Article Online
DOI: 10.1039/D0TA06865A

ARTICLE

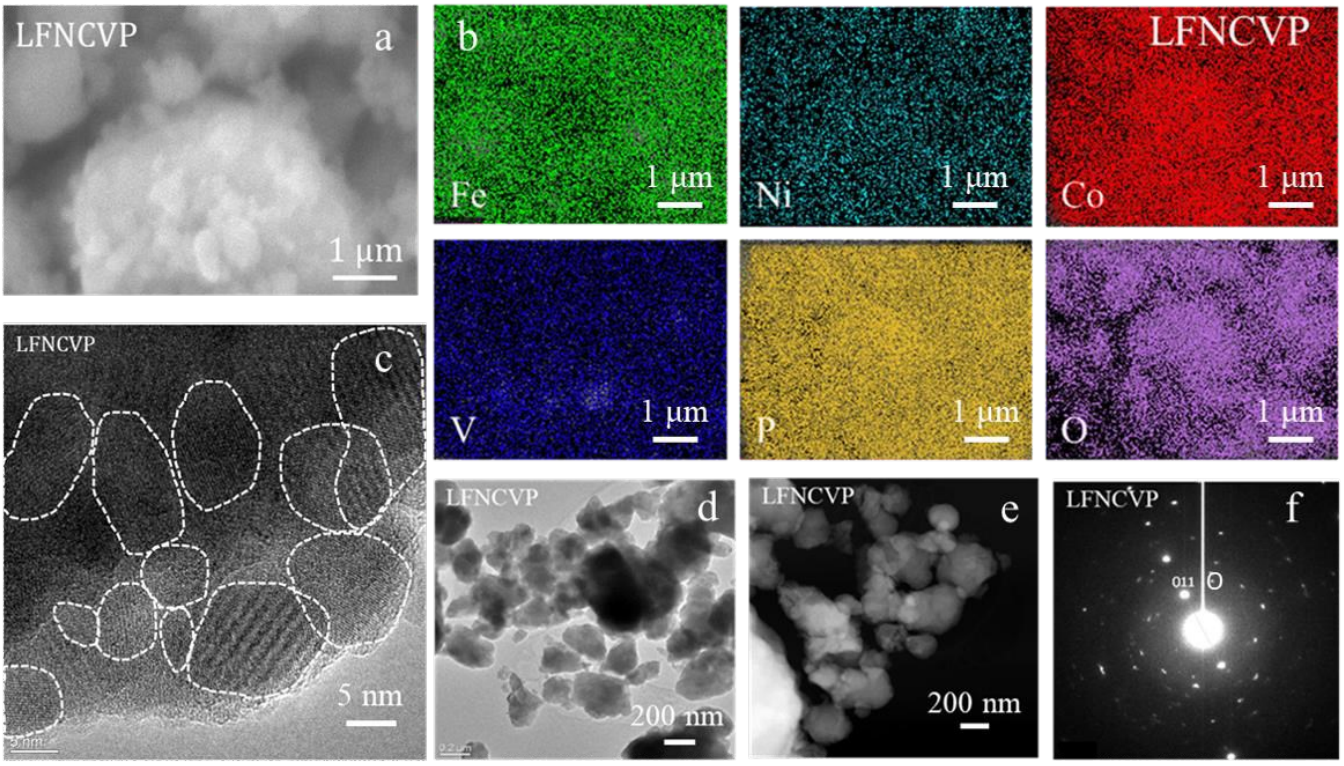

Fig. 1. Electron Microscopy images of LFNCVP sample. SEM image (a), EDX mapping (b), HR-TEM micrographs (c and d), STEM (e), and SAD image (f). In the figure Miller index is reported and O stands for Olivine.

Tab. 1. ICP-AES stoichiometry and crystal lattice parameters of the olivines with *Pnma* (62) space group.

Group	Sample	Synthesis	ICP-AES Results [a]	Rietveld Refinement				
				a / Å	b / Å	c / Å	V / Å^3	R_{wp} (%) [b]
A	LFNCVP	V/air	$Li_{1.09}Fe_{0.33}Ni_{0.07}Co_{0.55}V_{0.04}(PO_4)_{0.93}$	10.187	5.915	4.709	283.776	1.78
	LFNCVP/C	V+C/air	$Li_{1.00}Fe_{0.34}Ni_{0.07}Co_{0.57}V_{0.04}(PO_4)_{0.98}$	10.191	5.924	4.719	284.934	1.76
	LFNCVP/H	V/H_2	$Li_{1.06}Fe_{0.33}Ni_{0.07}Co_{0.55}V_{0.04}(PO_4)_{0.95}$	10.266	5.965	4.706	288.194	1.83
B	LFNCNP	Nb/air	$Li_{0.99}Fe_{0.34}Ni_{0.07}Co_{0.57}Nb_{0.04}(PO_4)_{0.94}$	10.198	5.912	4.712	284.089	1.61
	LFNCTP	Ta/air	$Li_{0.98}Fe_{0.35}Ni_{0.07}Co_{0.58}Ta_{0.04}(PO_4)_{0.97}$	10.184	5.924	4.709	284.094	1.85

[a] The error is ≤ 2 %; [b] R_{wp} is the weighted Rietveld index: $R^2_{wp}=\Sigma_i w_i(y_{C,i}-y_{O,i})^2/\Sigma_i w_i(y_{O,i})^2$, where w_i is the weight ($1/\sigma^2[y_{O,i}]$) and y_i the intensity calculated (C) or observed (O).[36]

Morphology and size distribution.

Fig. 1 shows the Scanning Electron Microscopy (SEM) results of a selected representative LFNCVP sample. The other cathodes present a similar morphology (see Fig. S3-S7, ESI†) which differs only in the size of nanoparticles, that shows a bi-modal distribution based on particles of few hundred nanometres supported on the surface of larger particles with an average size of few micrometres. Similar results are elsewhere reported for similar materials.[17, 18] In details, synthesis III gives rise to a cathode material (LFNCVP/H) based on particles with an average diameter of *ca*. 1 μm and with a more homogeneous particle size distribution. These evidences clearly demonstrate that the proposed synthetic routes influence both the composition and the morphology of the cathode materials. LFNCNP and LFNCTP (group B) show a morphology which is consistent with that of LFNCVP materials. However, it is to be noticed that within the same synthesis pathway, if we exclude the particle size distribution, no significant dependence of morphological features on the dopant ion (*i.e*. V, Nb, or Ta) is observed. Energy dispersive X-ray (EDX) maps (Fig. 1b and S4, ESI†) show that the elements composing the samples are uniformly distributed. A different behavior is revealed for the distribution of nickel and tantalum in LFNCVP/H and LFNCTP, respectively. Indeed, in LFNCVP/H material, only small Ni-rich olivine domains are revealed (no unreacted nickel oxide is observed, see Structure section). On the other hand, in LFNCTP segregated tantalum-based particles are detected which correspond to traces of unreacted tantalum(V) oxide (see Structure section). Taking all

together, results are in accordance with ICP-AES analyses (Tab. 1) and witness that the proposed synthesis protocol is very effective for the preparation of olivine-like materials.

High-resolution transmission electron microscopy (HR-TEM) studies allow to complete the investigation on the morphology and crystallinity of the obtained materials. Fig. 1c and d show the micrographs of LFNCVP cathode. Images of the other olivine samples are reported in the Supporting Information (Fig. S5, ESI†). The scanning transmission electron microscopy image (STEM) (Fig. 1e) is in accordance with SEM analyses. Indeed, HR-TEM micrographs reveal that the materials consist of nanoparticles based on nanocrystals with different orientations coalesced together. All these nanocrystals show the same structure (see highlighted regions of Fig. 1c). However, when no vicariant HVTM is inserted into the olivine structure,[18] their particles are based on nanocrystals with larger size.

Taking all together, the doping of olivine materials with HVTMs inhibits the growth of large single crystals and promotes the formation of particles based on coalesced crystalline nanodomains. The fringe periodicity of crystalline nanodomains can be determined by applying the Fast Fourier Transform (FFT) to the frequency distribution of the pixel intensities of HR-TEM images (Fig. S6, ESI†). In this way, each reflection can be Miller-indexed exactly. As expected, most of the observed reflections correspond to the structural features typical of the predominating olivine component. It is noticed that when lithium metal phosphates are based on a single HVTM, no olivine structure is observed. Indeed, with vanadium the monoclinic α-$Li_3V_2(PO_4)_3$ phase is formed which exhibits a $P2_1/n$ space group. This confirms that the optimized stoichiometry is crucial in order to obtain olivine systems with vicariant HVTMs. Hematite traces of unreacted Fe_2O_3 are also revealed in LFCNVP/C sample. Selected Area Diffraction (SAD) patterns (Fig. 1f and S7, ESI†) clearly reveal the presence of the olivine (011) reflection, which confirms that the proposed materials are endowed with a very high crystallinity.

Structure.

The study of the vibrational modes associated to the M-O and Li-O coordination bonds by Fourier Transform Infrared Spectroscopy (FT-IR) is crucial to investigate the structure and the interactions in materials. The FT-IR spectra in the 200÷1300 cm^{-1} range (Fig. S8, ESI†) are first baseline-corrected and then normalized to the peak centered at 957 cm^{-1}, which is attributed to the antisymmetric stretching of P-O bonds ($\upsilon_3([PO_4]^{3-})$). The correlative assignment of the FT-IR spectra of selected LFNCVP cathode is summarized in Tab. S1, ESI†. In the spectral region above 1300 cm^{-1} no peaks of ammonium and carbonate moieties are detected, demonstrating a complete consumption of the reagents during the synthesis of materials. In the 500÷1300 cm^{-1} range peaks attributed to the vibrational modes of $[PO_4]^{3-}$ tetrahedral groups are observed. The peak centered at *ca*. 1212 cm^{-1} is attributed to the presence of the diphosphate ion,[37, 38] which is absent in the LFNCVP/H sample (see Structure section). Below 500 cm^{-1}, peaks associated to the metal-oxygen and lithium-oxygen vibrational modes are observed.[39, 40] Phosphate ions are characterized by four vibrational modes: (i) the υ_1 singlet (A_1) at 940 cm^{-1}, which is assigned to the symmetric stretching of P-O bond; (ii) the triple degenerated υ_3 (F_2) mode at 1022 cm^{-1}, which is associated to the antisymmetric P-O stretching mode; (iii) the υ_2 doublet (E) at 427 cm^{-1}, which is attributed to the symmetric O-P-O bending vibration; and iv) the triple degenerated υ_4 (F_2) mode at 547 cm^{-1}, corresponding to the antisymmetric bending mode of O-P-O bond.[41] In a solid state material the so-called "*correlation effect*", which is observed when the asymmetric molecular units are located in some specific site symmetries, leads to the solid state splitting of their IR modes.[41] In details, in olivine materials a well-defined splitting of very intense bands is diagnostic of a high crystallinity of materials.[41] The peak splitting effect increases on the ionization energy of the element sitting in the center of the coordination octahedral site.[37] Therefore, the splitting of the band peaking at *ca*. 640 cm^{-1} is diagnostic of the insertion of a vicariant metal with a higher ionization energy into the structure of the proposed materials.[18] In details, a large band splitting value is expected also at low HVTM doping concentrations, when Co^{2+} (second ionization energy is 17.083 eV [42]) is replaced by V^{4+} (fourth ionization energy is 46.709 eV [42]), Nb^{5+} (fifth ionization energy is 50.55 eV [42]), or Ta^{5+} (fifth ionization energy is 45 eV [43]). This is confirmed by Fig. S8b, ESI†, which shows that, with respect to the reference sample (LFNCP), more pronounced peak splittings are detected in doped materials.[18] LFNCVP/H exhibits a lower splitting of the phosphate peaks in the whole spectral range. The broadening of these peaks is diagnostic of the decrease in lifetime of the phonon modes owing to the presence in materials of structural defects. Indeed, these latter are able to break the periodicity in the lattice of the olivine nanocrystallite domains, and thus to reduce the electrochemical performance of these systems.[44] Finally, a redshift of the Li-O vibrational mode ($468 \leq \bar{\upsilon} \leq 472$ cm^{-1}) is revealed in materials with respect to the reference cathode (LFNCP, 474 cm^{-1}) (Fig. S8c, ESI†).[18] This redshift is correlated to the presence in the olivine structure of vicariant high valence ions (*i.e*., V(IV), Nb(V), and Ta(V)), which acts to distort the lithium-oxygen coordination cage weakening the strength of their interactions. Therefore, a distorted cage of weaker Li-O coordination bonds would facilitate the Li^+ long-range migration during the insertion/de-insertion processes. On these bases, the lowest electrochemical performance is expected for LFNCVP/H, which presents the strongest Li-O bonds (smaller shift of υ(Li-O)).

The powder wide-angle X-ray diffraction spectra (WAXD) are used to study the crystalline phases present in the proposed materials and to investigate their structural evolution on synthesis conditions (group A) and ion doping effect (group B) (Fig. 2). The diffractograms of the samples shown in this figure are dominated by peaks typical of an olivine phase.[45] Small traces of byproducts and unreacted reagents such as Li_3PO_4,[46] Fe_2O_3,[47] $LiMP_2O_7$,[48] and Ta_2O_5[49] are also detected. A careful analysis of WAXD profiles permits to exclude the presence of NiO, V_2O_5, and Nb_2O_5 phases. A quantitative analysis of WAXD spectra is carried out by Rietveld method. For the sake of brevity, Fig. S9, ESI†, shows a selected refined result of LFNCVP sample. The *hkl* indexing of reflections of various phases of LFNCVP sample is summarized in Tab. S2, ESI†. Results confirm that the main phase present in proposed materials is an olivine ($LMPO_4$), exceeding at least the 92 wt% in all the samples, while each impurity phase accounts for less than 2.5 wt% (see Tab. S3, ESI†). Furthermore, in group A, iron, nickel, and cobalt ions are vicariant within the olivine structure, in accordance with other studies,[18] while the amount of byproducts and of unreacted reagents decreases on

View Article Online
DOI: 10.1039/D0TA06865A

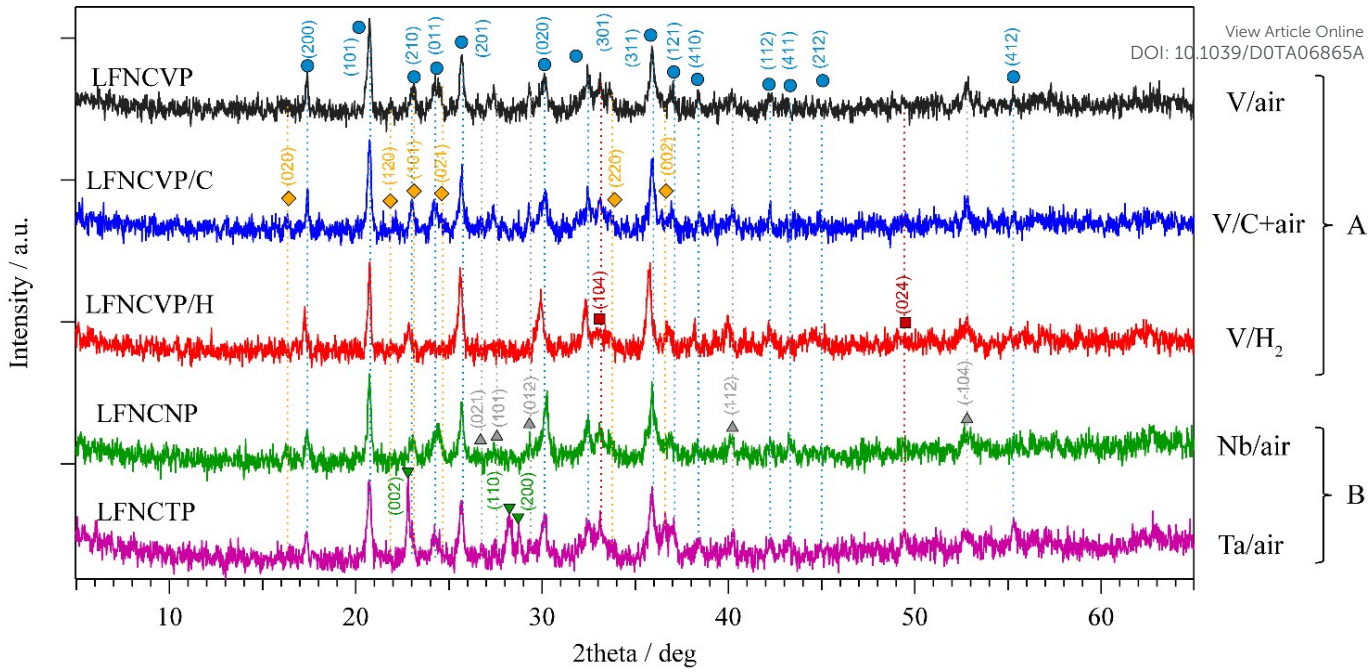

Fig. 2. Powder WAXD patterns of samples. Phases are labelled using different markers: ● $LiMPO_4$, ◆ Li_3PO_4, ■ Fe_2O_3, ▲ $LiMP_2O_7$, and ▼ Ta_2O_5.

the reducing environment in the order LFNCVP/H < LFNCVP/C < LFNCVP. However, in LFNCVP/H sample the olivine phase reaches a maximum value of 98.00 wt%. It should be noticed that vanadium and niobium are vicariant in the 3D olivine structure at a molar ratio M/P = 0.04 (M = V and Nb), while, for Ta, a M/P molar ratio of 0.02 is determined, considering the unreacted Ta_2O_5 phase which is still present into the sample. Typically, it is expected that the replacement in the 3D crystal structure of ions with different size and electronic configuration results in a modulation of lattice parameters and thus of the cell volume of materials. The structural results summarized in Tab. 1 show that the cell volume rises on increasing the reducing environment of the synthesis. This evidence is likely associated to the complete conversion of iron oxide into the desired olivine compound, which acts to reduce the fraction of reagent (*e.g.* Fe_2O_3) and byproduct (*e.g.* $LiMP_2O_7$) traces in samples. Indeed, iron, which exhibits the largest metal ion radius ($r_{Fe^{2+}}$ = 61 (Low–spin) / 78 pm (High-spin); $r_{V^{4+}}$ = 58 pm; $r_{Nb^{5+}} = r_{Ta^{5+}}$ = 64 pm),[18] is likely the main responsible for the increase of the cell volume. On the other hand, no significant change in volume is observed on doping the olivines with V, Nb, and Ta (group B) with respect to the reference undoped material (V = 284.056 Å^3),[18] which suggests that in this case no effect of HVTM dopant on lithium-ion diffusion in bulk 3D olivine material is expected. Taken all together, WAXD analyses allow to reveal that in the obtained cathode materials: a) the olivine-like phase is predominant; and b) the HVTMs M/P ≤ 0.04 are vicariant within the olivine crystal structure. In addition, in group A, the increase of reducing environment of the preparation protocol: (i) diminishes the concentration of byproducts; (ii) achieves an efficient utilization of the reagents; and (iii) increases the cell volume of materials. Finally, it should be noticed that only a slight variation of the cell volume is revealed in materials when a small fraction of Co is substituted by Nb or Ta (group B cathodes).

Electrochemical studies.

The "*ex-situ*" electrochemical performance of the obtained materials is studied using a three-electrode cell configuration by cyclic voltammetry (CV) in the potential range 3.5÷5.0 V *vs*. Li/Li$^+$. Lithium ribbons are used both as counter and reference electrodes, while a Pt wire covered with the active material is used as a working electrode (see Experimental section for more details). A 1.0 M solution of $LiPF_6$ in EC/DMC 1:1 V/V is used as electrolyte. CV profiles are shown in Fig. 3a and S10, ESI†. The oxidation process, which is revealed in the range 4.6 to 5.0 V *vs*. Li/Li$^+$, corresponds to the extraction of lithium ions from the 3D olivine cathodes. In the back scan, the opposite process is revealed, which involves Li$^+$ re-insertion inside the 3D olivine crystalline structure. It is observed that the oxidation event of transition metals takes place in a narrow potential window (*ca*. 4.60÷4.95), with a shoulder at lower potentials. This effect is more evident at low scan rates. On the other hand, the reduction processes occur within a broader potential range with two main peaks centered at *ca*. 4.2 and 4.9 V *vs*. Li/Li$^+$. In accordance with other studies, this non-symmetrical behavior of the redox events is attributed to the presence in materials of an average solid state electronic orbital which is the result of the concurring combination of all the electronic contributions of the transition metals (*i.e.*, Fe, Ni, Co, and V/Nb/Ta) composing the olivine structure.[18] Therefore, these redox events are not associated to a localized ion center, but they are attributed to the electrochemical behavior of an overall channel, whose red-ox features are modulated by the type of distribution of the vicariant transition metals along the insertion channel.[18] Indeed, the Fe(II/III) redox couple, that typically appears at +3.5 V for similar systems,[50] and the redox events attributed to the crystalline phase $Li_3V_2(PO_4)_3$, which are usually detected at 3.6, 3.7, 4.1, and 4.6 V,[51] are not observed, confirming that the dopant transition metals are vicariant within the olivine structure and that no segregated single-metal $LiMPO_4$ phases are present in proposed materials. The different current density values of the redox events exhibited by the

View Article Online
DOI: 10.1039/D0TA06865A

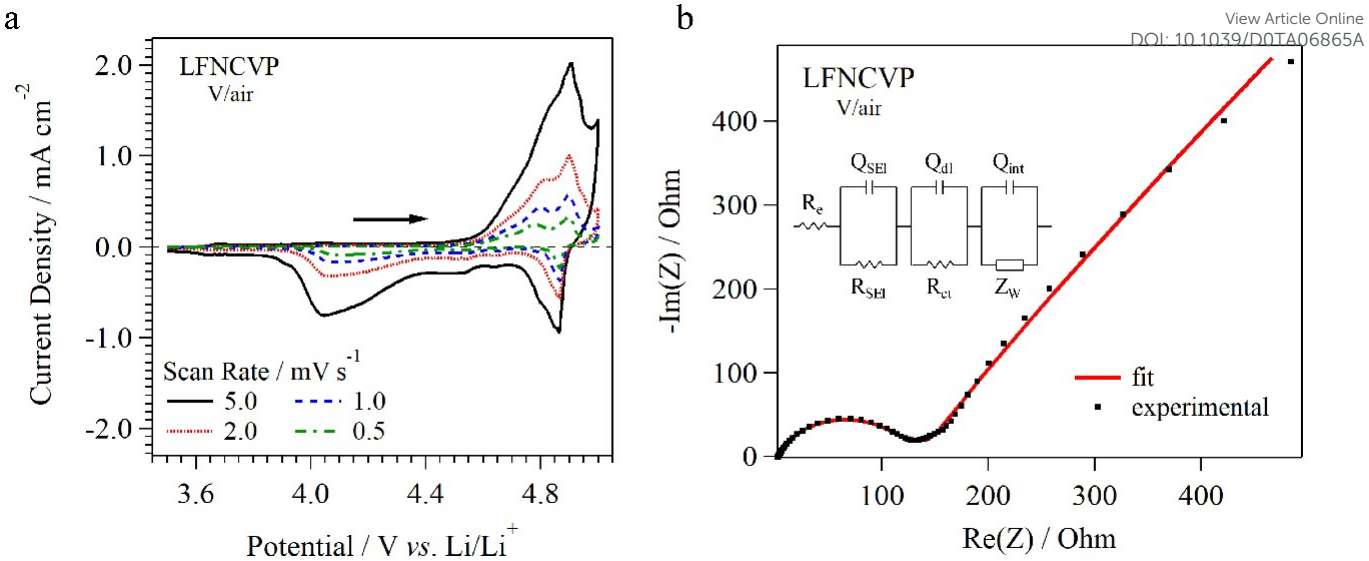

Fig. 3. CV profiles of LFNCVP material at different scan rates (a). The cathode is supported on a Pt wire. Lithium metal ribbons are used as reference and counter electrodes, and 1 M $LiPF_6$ in EC/DMC 1:1 as electrolyte. EIS spectrum of LFNCVP sample in a full-cell device (b). The equivalent circuit used for fitting is shown in the inset.

proposed samples witness that these systems are characterized by a different type of reactivity. The dependence of the oxidation and reduction current peak density (i_p) on the square root of the CV scan rate (v) shows a linear behavior (see Fig. S11, ESI†), which confirms that the electrochemical processes are under the mass transport control.[52] To determine the lithium ion diffusion coefficient (D_{Li}), the linear dependence of i_p *vs.* the v is fitted by Equation 3:[52]

$$i_p = 0.4463\left(\frac{F^3}{RT}\right)^{\frac{1}{2}} \cdot n^{3/2} \cdot A \cdot D_{Li}^{\frac{1}{2}} \cdot C_0^* \cdot v^{\frac{1}{2}} \quad (3)$$

where F is the Faraday constant, R the gas constant, T the temperature in Kelvin, n is the number of electrons exchanged during each redox process (*i.e.*, 1), A the electrode active surface in cm^2, D_{Li} the lithium ion diffusion coefficient in $cm^2\ s^{-1}$, and C_0^* the lithium ion concentration in mol cm^{-3}. The D_{Li} values summarized in Tab. S4 and Tab. S5, ESI†, are slightly lower than those reported in literature for similar olivine materials and the reference undoped sample.[17] At a first view, D_{Li} values should be higher for the HVTM-doped olivines, due to the weakening of the Li-O coordination interactions in the crystal channels. Nevertheless, the proposed cathodes are composed of very small olivine crystalline domains, which hinder their long-range connectivity inhibiting the Li^+ diffusion process in the materials. Overall, this latter effect predominates in the long-range migration phenomena of Li^+ ions during the insertion/de-insertion processes, thus a higher D_{Li} value is determined for the reference undoped sample (see Tab. S5, ESI†). For LFNCVP and LFNCNP materials, a higher electrochemical performance is expected in the battery tests on the basis of their higher D_{Li} values.

Further insights on the lithium ion migration processes within the obtained cathode materials are gathered by means of electrochemical impedance spectroscopy (EIS) studies. EIS measurements are performed "*in situ*" adopting a Li|electrolyte|cathode cell configuration with a 1.0 M $LiPF_6$ in EC/DMC (1:1 V/V) electrolyte. In order to reduce the effect of the interface resistance on the electrochemical response of the cell, AC impedance measurements are collected after ten galvanostatic cycles.[17] In this way, a consolidated SEI is formed and the maximum electrolyte flooding of interstitial free volume between cathode nanoparticles is obtained. Fig. 3b and S12, ESI†, show the measured Nyquist plots of the proposed materials. For the analysis of the Nyquist plots, after a careful evaluation of all the possible events responsible of the electrical response of materials, an equivalent circuit (see inset of Fig. 3b) perfectly in accordance with that used in literature for similar systems is assumed.[53] R_e element is attributed to the ohmic resistance of the electrolyte (Fig. 3b). Q_{SEI} and R_{SEI} are the SEI capacitance and resistance, respectively. R_{ct} and Q_{dl} are the charge transfer resistance and the double layer capacitance at the SEI/$LiMPO_4$ interface, respectively. Z_w and C_{int} are the Warburg impedance and the intercalation capacitance of lithium ions in olivines, respectively.

As elsewhere reported,[52] the exchange current density (i_0) is determined from R_{ct} values by using Equation 4:

$$i_0 = \frac{R \cdot T}{n \cdot F \cdot R_{ct}} \quad (4)$$

where R is the universal gas constant, T is the absolute temperature, n is the number of the electrons exchanged during each process (*i.e.*, 1), and F is the Faraday constant. A summary of the charge-transfer resistance and exchange current density values determined in this work is shown in Tab. S6, ESI†. LFNCVP and LFNCNP show the highest electrochemical performance. Indeed, they present low values of charge transfer resistances and the highest values of i_0. Results demonstrate that a reducing environment during the synthesis acts to increase the R_{ct} values of samples (see LFNCVP/C and LFNCVP/H in Tab. S6, ESI†). Concurrently, the lowest R_{SEI} value is obtained for LFNCVP sample, confirming that the oxidizing conditions must be preferred to achieved a more electrochemical stable condition. Therefore, the presence of byproduct traces on the surface of active LFNCVP and LFNCNP samples provides to these materials a protective layer which improves their charge transfer properties and stabilizes the SEI layer. This evidence is in accordance with results elsewhere reported,[17, 54-56] which show that metal oxides present at the interface between cathode nanoparticles and the electrolyte

DOI: 10.1039/D0TA06865A

boost the electrochemical kinetics of reactions.[17, 54-56] In particular, this layer inhibits the side reaction between the cathode and electrolyte associated with the increase of lithium ion conductivity. In our work, for LFNCVP and LFNCNP with respect to the purer LFNCVP/C and LFNCVP/H samples, this is reflected by: (i) the higher D_{Li} values; and (ii) the comparison of R_{SEI} values. These results corroborate the hypothesis of an improved stability at the electrode/electrolyte interface. If compared with the reference undoped LFNCP cathode material (see Tab. S6 in ESI†), higher R_{ct} values are obtained when high valence transition metals are inserted into the olivine structure. Indeed, as previously discussed for D_{Li} coefficient determined from CV experiments, the presence of smaller olivine crystalline domains acts to hinder the transport of electrons through the electrode|electrolyte interface at the single crystal fragment.

Furthermore, EIS spectroscopy is useful also in order to determine the lithium ion diffusion coefficient (D_{Li}) of olivines by using the following Equation:[17, 57-60]

$$D_{Li} = \frac{1}{2}\left[\left(\frac{V_m}{F \cdot S \cdot \sigma}\right)\left(\frac{dE}{dx}\right)\right]^2 \quad (5)$$

where V_m is the molar volume of the olivine material, F the Faraday constant, S the surface area of the electrode, σ the Warburg coefficient obtained by fitting EIS profiles, dE/dx the slope of the electrode potential (E) *vs*. composition evaluated from the galvanostatic curves. The D_{Li} values determined by using the two different techniques above described (*i.e*., EIS and CV), are in perfect accordance (see Tab. S5, ESI†). Taken all together, results on D_{Li} values suggest that: (i) an oxidizing atmosphere during the synthesis is the best choice to improve the performance of materials; (ii) in group A, no monotonic relationship exists between D_{Li} and the degree of reducing environment of pyrolysis process (the highest D_{Li} value is exhibited by LFNCVP, which is obtained under oxidative conditions); (iii) in group B, D_{Li} values increase in the order Ta < V < Nb, thus the best performance in galvanostatic cell cycling tests is expected for LFNCNP material; and (iv) with respect to the undoped material, the proposed cathodes show lower D_{Li} values since the gain, due to the weakening of Li-O interactions, is lower in magnitude with respect to the loss caused by the presence of smaller crystalline domains.

Battery tests.

To complete the electrochemical studies, the materials are tested in a CR2032 coin cell under galvanostatic conditions using lithium metal as anode. For durability tests, cells are charged and discharged between 3.5 and 5.0 V, at C/5 and 2C rates (1C = 170 mA g^{-1}), while, for the rate capability tests, they are cycled at different current rates (*i.e*. C/5→C/2→C→2C→5C→10C→C/5). Charge-discharge polarization curves are shown in Fig. S13, ESI†. It should be observed that, in correspondence to the potential of CV peaks, plateaus are revealed in polarization curves. This confirms that the "*ex-situ*" and "*in-situ*" methods are perfectly coinciding and that the proposed materials operate at high voltage. No remarkable variation in the cycling potential range is observed: (i) with respect to the reference LFNCP material;[18] (ii) in group A, as the reducing environment adopted in the synthesis process rises; and (iii) in group B, as V is substituted with Nb or Ta. Thus, the average charge and discharge potential depends on the type of transition metal combination dominating the composition of the olivine (*i.e*., cobalt, iron and nickel) and is not affected by the type of dopant ions or synthetic route used to prepare the materials. Over cycling, the obtained materials show a slight decay of capacity that stabilizes after *ca*. 40 cycles. This phenomenon which, with respect to the undoped LFNCP reference cathode[18] is more evident in proposed materials, can be explained on the basis of the typical slightly lower structural stability of the olivine systems. However, it cannot be excluded that the higher reactivity towards Li^+ insertion exhibited by the HVTMs doped olivine cathodes may also be responsible for the degradation of the electrolyte during the formation of the SEI. Indeed, the electrolyte oxidation starts at *ca*. 4.6 V[18] and likely this is the main drawback in the capacity fade observed during the first dozen of cycles. For each material, Fig. 4a shows its representative discharge curve, while Tab. 2 summarizes its capacity and energy values. Results of group A reveal that, both in terms of high discharge specific capacity and retained capacity after 150 cycles, the best performing cathode is LFNCVP. This material exhibits a maximum discharge specific capacity of 125 mAh g^{-1} and more than 60 % of capacity retention after 150 cycles. LFNCVP/C and LFNCVP/H samples show a maximum discharge specific capacity of 116 and 103

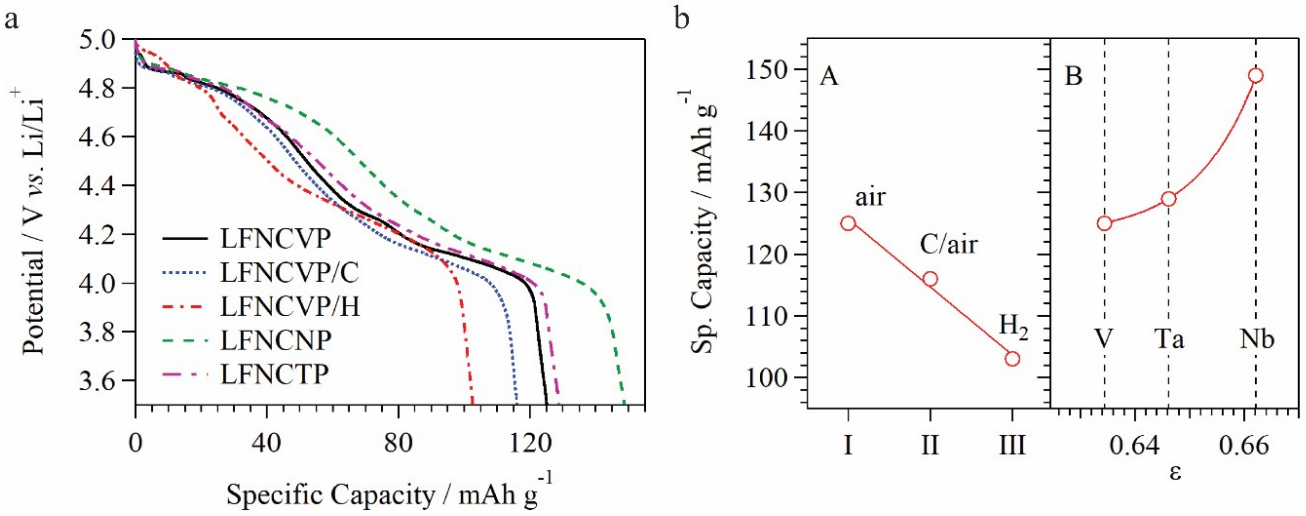

Fig. 4. Comparison between polarization curves of proposed materials at C/5, with C = 170 mA g^{-1} (a). Maximum specific capacity on synthesis conditions (group A) and charge compensation ratio, *ε*, (group B) (b).

Tab. 2. Specific capacity and energy values of obtained materials and reference cathode (R).[18]

Group	Sample	Specific capacity / mAh g^{-1}	Specific energy / mWh g^{-1}
A	LFNCVP	125	550
	LFNCVP/C	116	512
	LFNCVP/H	103	455
B	LFNCNP	149	656
	LFNCTP	129	568
R	LFNCP [a]	125	560

[a] LFNCP is the reference cathode material (R).[18]

mAh g^{-1}, respectively. After 150 cycles these values decrease down to *ca*. 72 and 65 mAh g^{-1} for LFNCVP/C and LFNCVP/H, respectively. It is interesting to notice that, in LFNCVP/C and LFNCVP/H samples, despite WAXD and HR- TEM analyses show a content of residues and by-products lower than LFNCVP, no improvements of their electrochemical performance are observed. The left panel of Fig. 4b shows that the specific capacity decreases linearly in the order I > II > III. In group B cathodes (right panel of Fig. 4b), it is revealed that niobium doping leads to the best cathode material obtained in this study. Indeed, a maximum specific discharge capacity of 149 mAh g^{-1} (656 mWh g^{-1}) is measured for LFNCNP sample, which after 150 cycles decreases to 93 mAh g^{-1}. This material in all the first 150 cycles shows a reversible Coulombic efficiency of *ca*. 100 %. With respect to LFNCNP material, LFNCTP sample presents a lower maximum specific discharge capacity (129 mAh g^{-1}), which is actually higher than that of LFNCVP and undoped LFNCP material (125 mAh g^{-1}). Furthermore, it is to be noticed that the specific capacity of group B cathodes (right panel of Fig. 4b) increases exponentially on the material's "*charge compensation parameter*" (ε):

$$\varepsilon = \frac{E_M - E_{Co}}{E_M} \qquad (6)$$

where E_M is the ionization energy of the HVTM in its most abundant oxidation state expected in the bulk (46.71, 50.55, and 48.27 eV for V^{4+}, Nb^{5+}, and Ta^{5+}, respectively) and E_{Co} is the ionization energy of cobalt(II) (17.08 eV).[61, 62] The exponential increase on ε of the specific capacity demonstrates that exists a monotonic correlation between the ionization energy of the dopant ion and the electrochemical performance. Therefore, the insertion of Nb^{5+} ion into the olivine structure perturbates significantly its electronic properties improving its lithium ion diffusion processes and specific capacity. The difference in specific capacity between LFNCNP and LFNCTP cathodes is attributed to three different concurring effects: (i) the presence of tantalum oxide which acts to reduce the specific capacity of the cathode material due to its inertia towards Li^+ insertion (even though the difference in the wt% of the olivine phase of *ca*. 1.8 is not enough to justify the lower specific capacity of LFNCTP sample); (ii) the lower doping amount of Ta into the olivine crystalline domains (M/P = 0.04 *vs*. 0.02) which gives rise to a lower charge compensation effect; and (iii) the presence of Ta_2O_5 impurity covering the olivine particles, which, on one hand is protecting the active material, and on the other side offers an excessive thick layer compromising Li^+ insertion process. LFNCNP and the undoped reference cathode material[18] demonstrate a similar and quite high Coulombic efficiency (*i.e.*, > 97 %), indicating that in these systems the charge compensation effect does not contribute to modulate this parameter. Moreover, they are both characterized by a protective layer which is formed during the synthesis under oxidative conditions. Nevertheless, the slightly lower cycle stability of LFNCNP can be assigned to its higher reactivity towards Li^+ insertion which is promoted by the HVTMs doping effect. The specific energy of proposed materials is higher than that of commercial cathodes. Indeed, the specific energy value of LCO and LFP are of *ca*. 520 mWh g^{-1},[63] and *ca*. 620 mWh g^{-1},[15] respectively. Nevertheless, if compared with the specific energy of NMC and NCA cathodes (*i.e.*, *ca*., 740 mWh g^{-1})[14] the here reported cathodes: (i) present a specific energy value slightly lower; and (ii) are cycling at a potential which is almost 1.0 V higher, thus they exhibit a higher specific power, which makes them very promising candidates for automotive applications. In summary, the here proposed cathodes show features which are clearly improved with respect to those of other similar recently published lithium - multi metal - phosphate olivine materials.[17, 18, 64] In addition,–the ability of the obtained materials to sustain high current densities during cycling maintaining a high capacity retention (rate capability) is studied. The significant enhancement in rate capability exhibited by the olivines doped with a HVTM is clearly evidenced in Fig. 5. Indeed, with respect to the reference LFNCP sample,[18] on the rate current the HVTM doped materials show a clear improvement in the specific discharge capacity. Thus, results demonstrate that the electron charge compensation effect plays a crucial role in improving the ability of proposed cathode materials to sustain very high currents, mitigating their capacity loss. A comparison between the rate capability properties of group A and group B cathodes is shown in Fig. S14, ESI†. It is revealed that in group A the rate capability is highly sensitive to the redox conditions adopted in the synthesis protocol. Particularly, LFNCVP shows a good specific discharge capacity even at high current rates (2C), while LFNCVP/C and LFNCVP/H present a decrease of the specific discharge capacity at high rates (Fig. S14a, ESI†). Only at 10C the difference between group A cathodes becomes negligible. The substitution in group B of vanadium with niobium or tantalum affects slightly their rate capability at moderated rates (*i.e.*, up to 2C), while at 5C and 10C the capacity retention of LFNCNP sample becomes remarkable with respect to that of the other cathodes (Fig. S14b, ESI†). It should be noted also that, at the same current rate (*i.e.*, 10C), the undoped

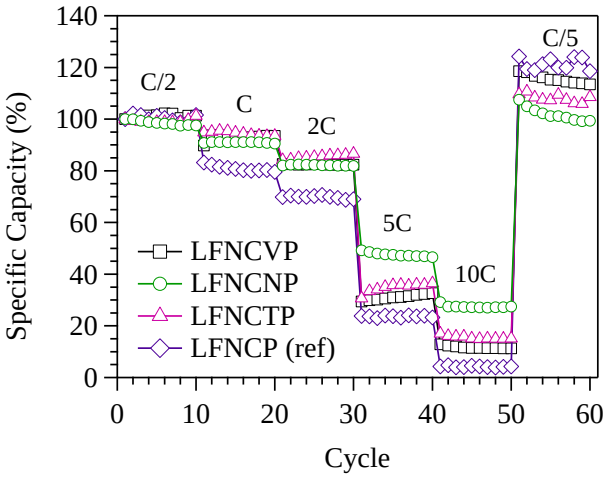

Fig. 5. Rate capability of the olivines doped with different HVTMs and of the undoped reference. 100 % of specific capacity corresponds to the discharge capacity of the first cycle at C/2.

reference cathode shows a residual capacity lower than the 5 % of the initial value, while LFNCNP still retains more than the 25 %.

Further studies on the capacity retention during long term cycling (*i.e.*, 500 cycles) at 2C rate of Group B cathodes are performed after an initial conditioning at low current rates (C/5), and results are shown in Fig S15, ESI†. The exhibited initial specific capacity is similar to that determined during the rate capability tests at 2C (Fig. S14b, ESI†). A reversibility higher than 98 % is maintained after 500 cycles for all the samples. The LFNCTP sample shows a partially stable performance in terms of discharge capacity which is comprised between LFNCNP (highest) and LFNCVP (lowest). The V-doped olivine cathode is characterized by a slight capacity decay over cycling, with a capacity retention of only 60 % after 500 cycles. On the contrary, the specific capacity of Nb-doped material is maintained almost constant for all the 500 cycles. The better cycling stability of this latter material can be explained considering two different hypotheses: (i) a higher content of byproducts in LFNCNP sample (see Tab S3, ESI†) which acts to protect the active material by enhancing its mechanical stability over cycling; and (ii) the higher charge compensation effect promoted by Nb doping with respect to V and Ta improves a longer cyclability at high current rates. Finally, the evolution of the morphology of the cycled LFNCNP cathode is studied by means of SEM microscopy after 300 cycles at 2C (see Fig. S16, ESI†). After cycling, the micro-porosity of the electrode is reduced. Reasonably, the electrochemical decomposition of the electrolyte leads to the formation of a layer which embeds the nanoparticles of the active materials. Indeed, a closer inspection of these materials reveals that the particles are covered by a multi-layered structure, which is consisting of degradation products of the electrolyte. The active material is still showing a bi-modal particle size distribution, in agreement with the pristine material (Fig. 1). Tacking all together, as previously hypothesized, the main cause of the capacity fade of the batteries must be attributed to the reduced electrochemical stability of the commercial electrolytes, which decompose forming a thick layer on the cathodic active particles, which is probably hindering the Li^+ insertion/de-insertion processes.

However, the capacity, working potential and rate capability of proposed materials is very promising for the development of secondary batteries for application in electric vehicles. It should be observed that the improvement of the rate capability of the cathode is one of the main goals to achieve in order to address the technical demands in applications of *next-generation* lithium batteries.

Experimental

Further details on the synthesis and the characterization techniques are summarized in the Electronic Supplementary Information. Briefly, in the first part of this work, three different solid-state syntheses were explored under: (a) a high oxidizing environment; (b) a mild reducing environment; and (c) a strongly reducing environment. In (a) procedure, the reagents are weighed in order to obtain an exact stoichiometry with a $Li:Fe:Ni:Co:V:PO_4$ molar ratio of *ca*. 1:0.34:0.07:0.55:0.04:1. Powders are preliminarily homogenized in an agate mortar and then ball milled in a planetary ball mill for 2 h at 500 rpm. The obtained mixture is sintered in a 20 mm diameter pellet under a pressure of 4 tons. The pellet is then pyrolyzed in an oven under air atmosphere at 700 °C for 24 h. Finally, the pellet is ground in a planetary ball mill for 2 h at 500 rpm to obtain the LFNCVP cathode material. In (b) the same preparation protocol of (a) pathway is used to obtain the LFNCVP/C cathode material except that, before the first ball milling process, an amount of 5 % by weight of XC-72R carbon black is added to the reagent mixture. Finally, in (c) the sintered pellet prepared as in (a) is placed into a closed quartz tube fluxed with Argon gas for 30 minutes to eliminate oxygen and moisture traces. The pellet is heated at 700 °C for 24 h under a H_2/N_2 (10:90 % V/V) gas mixture fluxed at *ca*. 0.5 L min^{-1}. After the pyrolysis, the product is slowly cooled down to ambient temperature under an Argon gas flow and then the resulting pellet is ground in a planetary ball mill for 2 h at 500 rpm to obtain the LFNCVP/H cathode material. Finally, following protocol (a) LFNCNP and LFNCTP cathodes are prepared by substituting V with Nb and Ta, respectively.

Conclusions

In this report, two strategies for the improvement of the performance of olivine cathode materials have been explored, namely the effect of the reducing environment during the synthesis (group A) and the influence of the nature of the dopant HVTM (group B). Both groups reveal a similar morphology and crystal structure, which differ from the undoped reference due to the presence of coalesced olivine nanocrystals with different orientations within the particles. In group A, the amount of by-products and unreacted reagents decreases on the reducing power of the synthesis. In addition, tantalum ions are only partially inserted into the structure since traces of Ta_2O_5 are detected. D_{Li} values obtained by means of CV and EIS studies reveal that oxidizing conditions must be preferred during the synthesis, and that the doping with HVTMs reduces the Li^+ insertion/de-insertion process kinetic. This is probably the result of the presence of smaller olivine crystalline domain within each nanoparticle. The best battery performance is achieved with the cathodes obtained under oxidizing conditions and, in particular, by the Nb-doped olivine (*i.e.*, a specific capacity of 149 mAh g^{-1} and a specific energy of 656 mWh g^{-1}). In addition, the doping with HVTMs gives rise to the electron charge compensation effect, which plays a crucial role in enhancing the rate capability of the proposed materials. Indeed, at 10C LFNCNP sample is able to provide more than 25 mAh g^{-1}, while the undoped LFNCP cathode only 5 mAh g^{-1}. Taking all together, the materials here described are extremely promising candidates for application in EVs, especially when high-voltage electrolytes for Li batteries will be available in the market.

Author contribution

V.D.N. proposed the research and coordinated the activities. E.N. and V.D.N. designed the experiments. G.P., M.B. and K.V. carried out the experiments. A.M. and V.M. performed and analyzed SEM, TEM and SAD measurements. R.B. conduct XPS characterizations. G.P., E.N. and V.D.N. wrote the paper. All the authors critically discussed

the results and commented on the manuscript. All authors approved the final version of the manuscript.

Conflicts of interest

There are no conflicts to declare.

Acknowledgements

This work was supported by the *"Centro Studi di Economia e Tecnica dell'Energia Giorgio Levi Cases"* of the University of Padova, the program *"Budget Integrato per la Ricerca Interdipartimentale - BIRD 2018"* of the University of Padova (protocol BIRD187913) and the program *"Progetti Di Ricerca Di Rilevante Interesse Nazionale - PRIN 2017"* (protocol 2017MCEEY4) funded by the Italian Ministry of Education, University and Research.

References

1. L. Liang, X. Sun, J. Zhang, L. Hou, J. Sun, Y. Liu, S. Wang and C. Yuan, *Adv. Energy Mater.*, 2019, **9**, 1802847.
2. L. Grande, E. Paillard, J. Hassoun, J.-B. Park, Y.-J. Lee, Y.-K. Sun, S. Passerini and B. Scrosati, *Adv. Mater.*, 2015, **27**, 784-800.
3. J.-S. Lee, S. Tai Kim, R. Cao, N.-S. Choi, M. Liu, K. T. Lee and J. Cho, *Adv. Energy Mater.*, 2011, **1**, 34-50.
4. V. Di Noto, S. Lavina, G. A. Giffin, E. Negro and B. Scrosati, *Electrochim. Acta*, 2011, **57**, 4-13.
5. H. Jung, R. Silva and M. Han, *World Electr. Veh. J.*, 2018, **9**, 46.
6. F. Bertasi, G. Pagot, K. Vezzù, A. Nale, G. Pace, Y. Herve Bang, G. Crivellaro, E. Negro and V. Di Noto, *Electrochim. Acta*, 2019, **307**, 51-63.
7. F. Bertasi, G. Pagot, K. Vezzù, E. Negro, P. J. Sideris, S. G. Greenbaum, H. Ohno, B. Scrosati and V. Di Noto, *J. Power Sources*, 2018, **400**, 16-22.
8. W. Huang, K. Yoshino, S. Hori, K. Suzuki, M. Yonemura, M. Hirayama and R. Kanno, *J. Solid State Chem.*, 2019, **270**, 487-492.
9. G. Pagot, F. Bertasi, K. Vezzù, G. Nawn, G. Pace, A. Nale and V. Di Noto, *Solid State Ion.*, 2018, **320**, 177-185.
10. B. W. Zewde, L. Carbone, S. Greenbaum and J. Hassoun, *Solid State Ion.*, 2018, **317**, 97-102.
11. S. Menkin, M. Lifshitz, A. Haimovich, M. Goor, R. Blanga, S. G. Greenbaum, A. Goldbourt and D. Golodnitsky, *Electrochim. Acta*, 2019, **304**, 447-455.
12. Y. Lu, Q. Zhang and J. Chen, *Sci. China Chem.*, 2019, **62**, 533-548.
13. J. Wang, X. He, E. Paillard, N. Laszczynski, J. Li and S. Passerini, *Adv. Energy Mater.*, 2016, **6**, 1600906.
14. R. Schmuch, R. Wagner, G. Hörpel, T. Placke and M. Winter, *Nature Energy*, 2018, **3**, 267.
15. Y. Wang, J. Wang, J. Yang and Y. Nuli, *Adv. Funct. Mater.*, 2006, **16**, 2135-2140.
16. J.-K. Kim, R. Vijaya, L. Zhu and Y. Kim, *J. Power Sources*, 2015, **275**, 106-110.
17. G. Pagot, F. Bertasi, G. Nawn, E. Negro, A. Bach Delpeuch, K. Vezzù, D. Cristofori and V. Di Noto, *Electrochim. Acta*, 2017, **225**, 533-542.
18. G. Pagot, F. Bertasi, G. Nawn, E. Negro, G. Carraro, D. Barreca, C. Maccato, S. Polizzi and V. Di Noto, *Adv. Funct. Mater.*, 2015, **25**, 4032-4037.
19. X. Fu, K. Chang, B. Li, H. Tang, E. Shangguan and Z. Chang, *Electrochim. Acta*, 2017, **225**, 272-282.
20. K. J. Kreder III, G. Assat and A. Manthiram, *Chem. Mater.*, 2016, **28**, 1847-1853.
21. J. Ma, B. Li, H. Du, C. Xu and F. Kang, *J. Electrochem. Soc.*, 2011, **158**, A26-A32.
22. C.-Y. Chiang, H.-C. Su, P.-J. Wu, H.-J. Liu, C.-W. Hu, N. Sharma, V. K. Peterson, H.-W. Hsieh, Y.-F. Lin, W.-C. Chou, C.-H. Lee, J.-F. Lee and B.-Y. Shew, *The Journal of Physical Chemistry C*, 2012, **116**, 24424-24429.
23. C. A. J. Fisher, V. M. Hart Prieto and M. S. Islam, *Chem. Mater.*, 2008, **20**, 5907-5915.
24. M. S. Islam, D. J. Driscoll, C. A. J. Fisher and P. R. Slater, *Chem. Mater.*, 2005, **17**, 5085-5092.
25. M. Wagemaker, B. L. Ellis, D. Lutzenkirchen-Hecht, F. M. Mulder and L. F. Nazar, *Chem. Mater.*, 2008, **20**, 6313-6315.
26. F. Omenya, N. A. Chernova, S. Upreti, P. Y. Zavalij, K.-W. Nam, X.-Q. Yang and M. S. Whittingham, *Chem. Mater.*, 2011, **23**, 4733-4740.
27. F. Wang, J. Yang, Y. NuLi and J. Wang, *J. Power Sources*, 2010, **195**, 6884-6887.
28. J. F. Moulder and J. Chastain, *Handbook of x-ray photoelectron spectroscopy: a reference book of standard spectra for identification and interpretation of XPS data*, Physical Electronics Division, Perkin-Elmer Corp., Eden Prairie, MN, USA, 1992.
29. T. Yamashita and P. Hayes, *Appl. Surf. Sci.*, 2008, **254**, 2441-2449.
30. A. Mansour and R. A. Brizzolara, *Surf. Sci. Spectra*, 1996, **4**, 345-350.
31. M. C. Biesinger, B. P. Payne, A. P. Grosvenor, L. W. Lau, A. R. Gerson and R. S. C. Smart, *Appl. Surf. Sci.*, 2011, **257**, 2717-2730.
32. S. Nordlinder, A. Augustsson, T. Schmitt, J. Guo, L. C. Duda, J. Nordgren, T. Gustafsson and K. Edström, *Chem. Mater.*, 2003, **15**, 3227-3232.
33. G. Silversmit, D. Depla, H. Poelman, G. B. Marin and R. De Gryse, *J. Electron. Spectrosc. Relat. Phenom.*, 2004, **135**, 167-175.
34. P. Zhang, Y. Wang, M. Lin, D. Zhang, X. Ren and Q. Yuan, *J. Electrochem. Soc.*, 2012, **159**, A402-A409.
35. E. Atanassova, T. Dimitrova and J. Koprinarova, *Appl. Surf. Sci.*, 1995, **84**, 193-202.
36. B. H. Toby, *Powder Diffr.*, 2006, **21**, 67-70.
37. A. A. Salah, P. Jozwiak, J. Garbarczyk, K. Benkhouja, K. Zaghib, F. Gendron and C. M. Julien, *J. Power Sources*, 2005, **140**, 370-375.
38. C. M. Julien, P. Jozwiak and J. Garbarczyk, Sofia, Bulgaria, 2004.
39. M. T. Paques-Ledent and P. Tarte, *Spectrochimica Acta Part A: Molecular and Biomolecular Spectroscopy*, 1974, **30**, 673-689.
40. W. Paraguassu, P. T. C. Freire, V. Lemos, S. M. Lala, L. A. Montoro and J. M. Rosolen, *Journal of Raman Spectroscopy*, 2005, **36**, 213-220.

Journal of Materials Chemistry A ARTICLE

View Article Online
DOI: 10.1039/D0TA06865A

41. C. M. Julien, A. Mauger, K. Zaghib, R. Veillette and H. Groult, *Ionics*, 2012, **18**, 625-633.
42. W. M. Haynes, *CRC Handbook of Chemistry and Physics, 93rd Edition*, Taylor & Francis, Boca Raton, FL, USA, 2012.
43. R. J. H. Clark, D. Brown, J. C. Bailar, H. J. Emeléus and R. Nyholm, *The Chemistry of Vanadium, Niobium and Tantalum*, Pergamon Press, Oxford, UK, 2013.
44. N. Ravet, M. Gauthier, K. Zaghib, Goodenough, A. Mauger, F. Gendron and Julien, *Chem. Mater.*, 2007, **19**, 2595-2602.
45. T. Kimura, C. K. Chang, F. Kimura and M. Maeyama, *J. Appl. Crystallogr.*, 2009, **42**, 535-537.
46. R. W. G. Wyckoff, *The Structure of Crystals: Supplement for 1930-1934 to the Second Edition*, Reinhold Publishing Corporation, Hoboken, NJ, USA, 1935.
47. L. Pauling and S. B. Hendricks, *J. Am. Chem. Soc.*, 1925, **47**, 781-790.
48. D. Riou, N. Nguyen, R. Benloucif and B. Raveau, *Mater. Res. Bull.*, 1990, **25**, 1363-1369.
49. L. Aleshina and S. Loginova, *Crystallography Reports*, 2002, **47**, 415-419.
50. J. Liu, M. N. Banis, Q. Sun, A. Lushington, R. Li, T. K. Sham and X. Sun, *Adv. Mater.*, 2014, **26**, 6472-6477.
51. M. Ren, Z. Zhou, Y. Li, X. P. Gao and J. Yan, *J. Power Sources*, 2006, **162**, 1357-1362.
52. A. J. Bard and L. R. Faulkner, *Electrochemical Methods: Fundamentals and Applications, 2nd Edition*, John Wiley & Sons, Hoboken, NJ, USA, 2nd edn., 2000.
53. Z. P. Cai, Y. Liang, W. S. Li, L. D. Xing and Y. H. Liao, *J. Power Sources*, 2009, **189**, 547-551.
54. L. Wang, X. Jie, G. Liang and X. Ou, *Adv. Mat. Res.*, 2012, **347-353**, 3443-3447.
55. Y. Cui, X. Zhao and R. Guo, *J. Alloys Compd.*, 2010, **490**, 236-240.
56. Q. Hao, H. Ma, Z. Ju, G. Li, X. Li, L. Xu and Y. Qian, *Electrochim. Acta*, 2011, **56**, 9027-9031.
57. C. Ho, I. D. Raistrick and R. A. Huggins, *J. Electrochem. Soc.*, 1980, **127**, 343-350.
58. J. Xie, K. Kohno, T. Matsumura, N. Imanishi, A. Hirano, Y. Takeda and O. Yamamoto, *Electrochim. Acta*, 2008, **54**, 376-381.
59. J. Xie, T. Tanaka, N. Imanishi, T. Matsumura, A. Hirano, Y. Takeda and O. Yamamoto, *J. Power Sources*, 2008, **180**, 576-581.
60. K. Dokko, M. Mohamedi, M. Umeda and I. Uchida, *J. Electrochem. Soc.*, 2003, **150**, A425-A429.
61. J. E. Huheey, E. A. Keiter and R. L. Keiter, *Inorganic Chemistry: Principles of Structure and Reactivity*, HarperCollins, New York, USA, 4th edn., 1993.
62. J. A. Dean, *Lange's Handbook of Chemistry*, McGraw-Hill, New York, USA, 14th edn., 1992.
63. R. Koksbang, J. Barker, H. Shi and M. Y. Saïdi, *Solid State Ion.*, 1996, **84**, 1-21.
64. D. Di Lecce, R. Brescia, A. Scarpellini, M. Prato and J. Hassoun, *ChemSusChem*, 2016, **9**, 223-230.

View Article Online
DOI: 10.1039/D0TA06865A

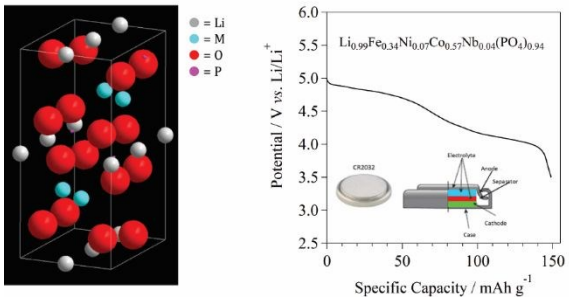

High-valence transition metals are inserted into an olivine structure, thus enhancing the specific capacity and rate capability of cathodic materials.